


## Effect of Ag incorporation on structure and optoelectronic properties of $(\text{Ag}_{1-x}\text{Cu}_x)_2\text{ZnSnSe}_4$ solid solutions

Galina Gurieva,<sup>1,\*</sup>† José A. Márquez,<sup>1,\*</sup>‡ Alexandra Franz,<sup>1</sup> Charles J. Hages,<sup>1,2</sup> Sergiu Levcenko <sup>1</sup>, Thomas Unold,<sup>1</sup> and Susan Schorr<sup>1,3</sup>

<sup>1</sup>Helmholtz Zentrum Berlin für Materialien und Energie GmbH, Hahn-Meitner-Platz 1, D-14109 Berlin, Germany

<sup>2</sup>Department of Chemical Engineering, University of Florida, 1006 Center Drive, Gainesville, Florida 32611, USA

<sup>3</sup>Institute of Geological Sciences, Free University Berlin, Malteserstrasse 74-100 Berlin, Germany



(Received 6 November 2018; revised manuscript received 15 July 2019; accepted 15 April 2020; published 20 May 2020)

The performance of  $\text{Cu}_2\text{ZnSnSe}_4$  solar cells is presently limited by low values of open-circuit voltage which are a consequence of strong band tailing and high level of nonradiative recombination. Recently, the partial substitution of Cu, Zn, and Sn by other elements has shown the potential to overcome this limitation. We explored the structural changes and the effect on the optoelectronic properties of the partial substitution of Cu with Ag in  $\text{Cu}_2\text{ZnSnSe}_4$ . This paper clarifies the crystal structure of  $(\text{Ag}_{1-x}\text{Cu}_x)_2\text{ZnSnSe}_4$  solid solution series, deducing possible cationic point defects and paying special attention to the presence of Cu/Zn disorder with a combination of neutron and x-ray diffraction. The optoelectronic properties of the solid solution series are assessed using reflection and quantitative photoluminescence spectroscopy, which allows us to estimate the fraction of nonradiative recombination, which would contribute to the open-circuit voltage loss in devices. The results strongly suggest Ag incorporation as a promising route to eliminate Cu/Zn disorder and to reduce nonradiative recombination losses in  $\text{Cu}_2\text{ZnSnSe}_4$ .

DOI: [10.1103/PhysRevMaterials.4.054602](https://doi.org/10.1103/PhysRevMaterials.4.054602)

### I. INTRODUCTION

The efficiency level of  $\text{Cu}_2\text{ZnSn}(\text{S}, \text{Se})_4$  (CZTSSe) kesterite solar cells is presently below 13% with the main loss in performance being attributed to low values of the open circuit (OC) voltage ( $V_{\text{OC}}$ ) [1]. The  $V_{\text{OC}}$  in CZTSSe devices is believed to be limited by significant nonradiative recombination [2], low minority carrier lifetime [3], and band-gap fluctuations partially caused by the exceptionally high density of antisite defects [4]. One of the recently tested strategies to overcome this limitation has been the partial replacement of Cu, Zn, and Sn cations by other elements. Successful examples of this have been demonstrated with the partial replacement of Cu, Zn, and Sn cations with Na, K, Li, Ag, Cd, and Ge [5–12]. By replacing Cu in CZTSe with Ag, whose covalent radius is 15% larger than that of Cu and Zn, the density of I–II antisite defects (e.g., Cu/Zn disorder) is predicted to drop helping to reduce the band tailing in the absorber [13].  $\text{Cu}_2\text{ZnSnSe}_4$  solar cells with Ag alloying recently reached an efficiency of 10.2% [10].  $\text{Cu}_2\text{ZnSnSe}_4$  and  $\text{Ag}_2\text{ZnSnSe}_4$  are quaternary semiconductors belonging to the adamantine compound family. It was shown by neutron diffraction that CZTSe crystallizes in the kesterite-type structure (space-group  $I4$ ) [14]. This structure can be derived from the cubic-sphalerite-type structure by doubling the unit cell in the direction of the

crystallographic  $c$  axis and an ordering of the cations. Very similar to the kesterite-type structure is the stannite-type structure (space-group  $I42m$ ). Besides the difference in the anion position, the main difference between these two structures lies in the cation distribution, especially with respect to  $\text{Cu}^+$  and  $\text{Zn}^{2+}$ . A differentiation between the isoelectronic cations  $\text{Cu}^+$  and  $\text{Zn}^{2+}$  and, consequently, between the kesterite- and the stannite-type structures as well as the information on Cu/Zn disorder in the kesterite-type structure is not possible using x-ray diffraction (XRD) due to their similar scattering factors. However, neutron diffraction can solve this problem as the coherent scattering lengths are sufficiently different for these cations [14]. In the case of  $\text{Ag}_2\text{ZnSnSe}_4$ , according to density functional theory calculations, the kesterite-type structure is considered as the ground-state structure [13]. Experimentally only x-ray diffraction was used until now to determine the crystal structure of AZTSe, and the kesterite structure was found [15]. But, in the case of  $(\text{Ag}_{1-x}\text{Cu}_x)_2\text{ZnSnSe}_4$ , a combination of neutron and x-ray diffraction is necessary in order to determine the cation distribution in these compounds.  $\text{Cu}^+$  and  $\text{Ag}^+$  are not isoelectronic, and  $\text{Ag}^+$  can be located by laboratory-based x-ray-diffraction measurements, but the problem of  $\text{Cu}^+$  and  $\text{Zn}^{2+}$  being isoelectronic remains. This paper presents a neutron diffraction based investigation of the crystal structure of  $(\text{Ag}_{1-x}\text{Cu}_x)_2\text{ZnSnSe}_4$ .

The aim of this paper is to clarify the crystal structure as well as to deduce possible cationic point defects, paying a special attention to the presence of Cu/Zn disorder in these compounds. Additionally, the optoelectronic properties of the synthesized powder materials are characterized by means of

\*These authors contributed equally to this work.

†galina.gurieva@helmholtz-berlin.de

‡jose.marquez\_prieto@helmholtz-berlin.de

hyperspectral imaging techniques, allowing us to evaluate the band gap and the quasi-Fermi-level splitting as a function of Ag substitution.

## II. EXPERIMENT

### A. Synthesis

The silver-containing compounds were synthesized via a solid-state reaction starting with the stoichiometric amounts of pure elements Ag (6*N*), Cu (6*N*), Zn (6*N*), Sn (6*N*), and Se (5*N*) in evacuated silica tubes, similar to the synthesis of CZTSe, CZGSe, and CZTS compounds [14,16,17–19]. Due to the comparably low decomposition temperature of the  $\text{Ag}_2\text{ZnSnSe}_4$  end member of the  $(\text{Ag}_{1-x}\text{Cu}_x)_2\text{ZnSnSe}_4$  solid solution [15], the maximum synthesis temperature had to be adjusted significantly, and, accordingly, the holding times had to be increased. As a result, the samples were synthesized using the temperature regime: 10 K/h to 200 °C hold for 24 h, 10 K/h to 400 °C hold for 24 h, 10 K/h to 550 °C hold for 20 days followed by natural cooling. The homogenization procedure—grinding in agate mortar, pressing in a pellet, and annealing at 550 °C for 20 more days, was repeated twice.

### B. Compositional characterization

To determine the chemical composition and phase content of the samples, wavelength dispersive x-ray spectroscopy (WDX) has been performed using an electron microprobe analysis system (JEOL-JXA 8200) equipped with a WDX unit where the phase content and chemical composition have been determined. In order to obtain reliable results from the WDX measurements, the system was calibrated using elemental standards. High accuracy of the compositional parameters was achieved by averaging over 20 local measurement points within one grain and averaging over 30 grains of the ACZTSe phase in the samples. Averaging over all grains of the main phase is possible due to the fact that deviations of the values for each of the measurements within each grain as well as among all of the grains did not exceed a 1% error, originating from the instrumental error.

### C. Structural characterization

For structural characterization of these mixed crystals, both neutron and x-ray diffraction were used. A PANalytical X'Pert PRO MRD diffractometer with Bragg-Brentano geometry and a sample spinner stage were used for the XRD measurements. The collected XRD patterns were further processed by a Rietveld refinement using the FULLPROF SUITE software package [23]. The Thompson-Cox-Hastings pseudo-Voigt function was applied to describe the XRD peak shape profile [20]. In order to distinguish between  $\text{Cu}^+$  and  $\text{Zn}^{2+}$ , neutron-diffraction experiments have been performed at the Berlin Research Reactor BER II at the Helmholtz-Zentrum Berlin für Materialien und Energie using the fine resolution powder diffractometer FIREPOD (E9) ( $\lambda = 1.7982 \text{ \AA}$ , ambient temperature) [21]. The data treatment was performed by a full pattern Rietveld refinement [22] using the FULLPROF SUITE software package [23].

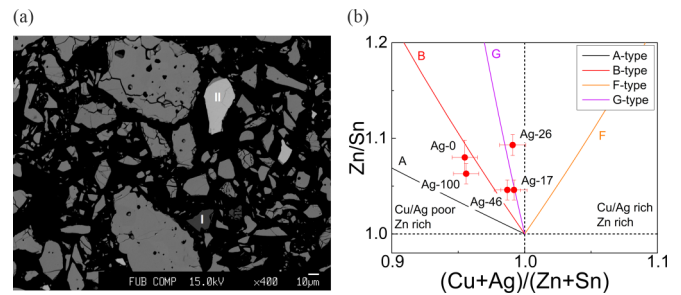


FIG. 1. (a) Backscatter electron (BSE) micrograph of the  $\text{Ag}_{0.91}\text{Cu}_{1.08}\text{Zn}_{1.03}\text{Sn}_{0.99}\text{Se}_4$  (Ag-46) sample with exemplarily grains belonging to secondary phases indicated: ZnSe darker grain I,  $\text{Ag}_6\text{SnSe}_8$  lighter grain II; (b) cation ratio plot  $(\text{Ag} + \text{Cu})/(\text{Zn} + \text{Sn})$  vs  $\text{Zn}/\text{Sn}$  showing the different off-stoichiometry types A, B, G, and F relevant for this paper [16,17,24]. The positions of the synthesized ACZTSe phases, obtained from the analysis of the WDX data are indicated.

### D. Characterization of the optoelectronic properties

The characterization of the optoelectronic properties was performed with a home-built hyperspectral imaging setup. The photoluminescence (PL) image detection was performed with a CCD camera for the AZTSe sample and with an InGaAs camera for the  $(\text{Ag}_{1-x}\text{Cu}_x)_2\text{ZnSnSe}_4$  with  $x = 0, 0.17, 0.26,$  and  $0.46$ . Both cameras are coupled to liquid-crystal tunable filters. The excitation for the CCD camera system was performed with two 455-nm light-emitting diodes equipped with diffuser lenses with an intensity of  $1.2 \times 10^{21}$  photons  $\text{m}^{-2}\text{s}^{-1}$ . The excitation for the InGaAs camera system was performed with two 660-nm fiber coupled lasers attached to homogenizers units with an intensity of  $4.8 \times 10^{21}$  photons  $\text{m}^{-2}\text{s}^{-1}$ . Both systems were calibrated to absolute photon numbers. The external PL quantum efficiency values are calculated from the ratio of total photons emitted to total photons absorbed. We assume that the absorptivity  $A$  equals 1 for the excitation wavelength used in this paper. The Shockley-Queisser (SQ) quasi-Fermi-level splitting ( $\Delta\mu^{\text{SQ}}$ ) values have been calculated by detailed balanced using the “AM 1.5 GT” solar spectrum. The calculations assume a steplike absorptivity function where all the photons above the band-gap value are absorbed. The calculated  $\Delta\mu^{\text{SQ}}$  vs band gap  $E_g$  is shown in the Supplemental Material [27]. For the calculation of the quasi-Fermi-level splitting values ( $\Delta\mu$ ), we assumed steplike absorptivity where  $A = 1$  for photon energies above the band gap and  $A = 0$  below the band gap.

## III. RESULTS AND DISCUSSION

The presence of small amounts of two secondary phases (ZnSe and  $\text{Ag}_6\text{SnSe}_8$ ) was detected in all of the Ag-containing samples. Additionally,  $\text{SnSe}_2$  was found in the AZTSe sample. The presence of secondary phases was the reason for the resulting off-stoichiometric compositions of the ACZTSe phase in contrast to the aimed stoichiometric compositions. Figure 1(a) presents a BSE micrograph showing the homogeneity of the main phase alongside with the presence of the two secondary phases which were as well detected with Raman spectroscopy (see the Supplemental Material part A [27]).

TABLE I. Overview of synthesized samples: cation ratios  $(\text{Ag} + \text{Cu})/(\text{Zn} + \text{Sn})$ ,  $\text{Ag}/(\text{Ag} + \text{Cu})$ , and  $\text{Zn}/\text{Sn}$  of the main phase obtained from the WDX analysis, chemical formula, off-stoichiometry type, and the presence of secondary phases.

Name	$(\text{Ag} + \text{Cu})/(\text{Zn} + \text{Sn})$	Zn/Sn	Ag/ (Ag + Cu)	Secondary phases	Final formula	Type
Ag-100	0.96 (1)	1.06 (1)	1.00	$\text{Ag}_8\text{SnSe}_6$ ZnSe SnSe <sub>2</sub>	$\text{Ag}_{1.95}\text{Zn}_{1.05}\text{Sn}_{0.99}\text{Se}_4$	A-B
Ag-46	0.99 (1)	1.05 (1)	0.46 (1)	$\text{Ag}_8\text{SnSe}_6$ ZnSe	$\text{Ag}_{0.91}\text{Cu}_{1.08}\text{Zn}_{1.03}\text{Sn}_{0.99}\text{Se}_4$	B-G
Ag-26	0.99 (1)	1.09 (1)	0.26 (1)	$\text{Ag}_8\text{SnSe}_6$ ZnSe	$\text{Ag}_{0.52}\text{Cu}_{1.48}\text{Zn}_{1.03}\text{Sn}_{0.99}\text{Se}_4$	G-F
Ag-17	0.99 (1)	1.05 (1)	0.17 (1)	$\text{Ag}_8\text{SnSe}_6$ ZnSe	$\text{Ag}_{0.35}\text{Cu}_{1.66}\text{Zn}_{1.06}\text{Sn}_{0.97}\text{Se}_4$	G
Ag-0	0.96 (1)	1.08 (1)	0.00		$\text{Cu}_{1.95}\text{Zn}_{1.06}\text{Sn}_{0.98}\text{Se}_4$	A-B

In addition, the Raman characterization part provides results concerning the effect of the Cu substitution by Ag on the Raman-active phonon modes in ACZTSSe samples. One of the samples (Ag-26) showed a few grains of a quaternary phase with slightly different  $\text{Ag}/(\text{Ag} + \text{Cu})$  ratios in addition to the quaternary main phase, which made it unsuitable for detailed structural characterization via neutron diffraction. In the case of the other ACZTSe powder samples (further referred to as Ag-17, Ag-46, and Ag-100), their main quaternary phases were homogeneous but with slightly off-stoichiometric composition [see Fig. 1(b)]. All of the ACZTSe phases were slightly Zn rich and Sn poor, whereas the  $(\text{Ag} + \text{Cu})/(\text{Zn} + \text{Sn})$  ratio is changing from 0.96 for CZTSe and AZTSe to 0.99 for the rest of the samples but remained very close to 1.

The  $(\text{Ag} + \text{Cu})/(\text{Zn} + \text{Sn})$ ,  $\text{Ag}/(\text{Ag} + \text{Cu})$ , and  $\text{Zn}/\text{Sn}$  ratios of the mixed crystals as well as the off-stoichiometry-type information and final formulas of the quaternary compounds, calculated according to the method described in Refs. [14,16,25], are presented in Table I.

Due to the similarity between the neutron-scattering length of Ag and Zn ( $b_{\text{Zn}} = 5.680$  and  $b_{\text{Ag}} = 5.922$  fm [26]) it is hard to distinguish them using only neutron scattering. In order to obtain reliable site occupancy parameters for all four crystallographic sites of the kesterite-type structure and locate

all four cations within the crystal structure, a simultaneous Rietveld refinement of x-ray- and neutron-diffraction data was performed. As the starting crystal structure model for the ACZTSe main phase, the kesterite-type structure (space-group  $I\bar{4}$ ) with Cu/Ag on  $2a:(0,0,0)$ , Cu on  $2c:(0, \frac{1}{2}, \frac{1}{4})$ , Zn on  $2d:(0, \frac{1}{2}, \frac{3}{4})$ , Sn on  $2b:(\frac{1}{2}, \frac{1}{2}, 0)$ , and Se on  $8g:(x, y, z)$  Wyckoff positions [14,15] was selected. Both secondary phases deduced from chemical analysis (WDX) have been included in the refinement files [see Fig. 2(a)]. The obtained phase contents are presented in the Supplemental Material in Table S1 [27]. The refinements have been performed without any chemical constraints. The resulting lattice constants are in a good agreement with Vegard's law [see Fig. 2(b), Table S1].

The Ag-46 sample is being discussed here in detail, as an example, whereas the same type of analysis was performed for all of the samples, and the results are presented in the Supplemental Material (Fig. S7) [27]. In order to determine the distribution of the cations  $\text{Cu}^+$ ,  $\text{Ag}^+$ ,  $\text{Zn}^{2+}$ , and  $\text{Sn}^{4+}$  on the four cation sites of the kesterite-type structure the method of the average neutron-scattering length analysis [28] was applied. The experimental average neutron-scattering lengths of the four cation sites  $2a$ ,  $2b$ ,  $2c$ , and  $2d$  were calculated as described earlier [17,19,28]. As the result of the compar-

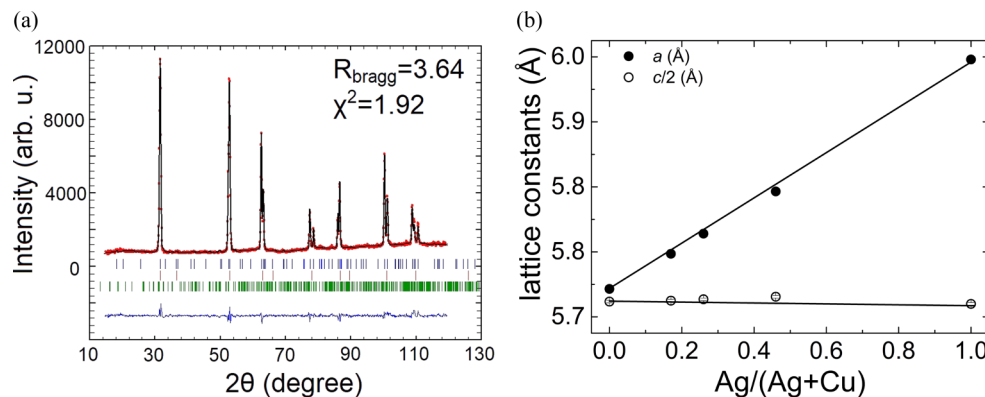


FIG. 2. (a) Rietveld refinement of the neutron-diffraction data for  $\text{Ag}_{0.35}\text{Cu}_{1.66}\text{Zn}_{1.06}\text{Sn}_{0.97}\text{Se}_4$  where the red dots are experimental data, the black line is the obtained fit, the blue ticks are the Bragg peak positions of the stannite-type structure, the red ticks are for ZnSe, the green ticks are for  $\text{Ag}_8\text{SnSe}_6$  secondary phases, and the blue line is the difference between the experimental and the calculated data; (b) lattice parameters  $a$  and  $c/2$  in dependence of the  $\text{Ag}/(\text{Ag} + \text{Cu})$  ratio.

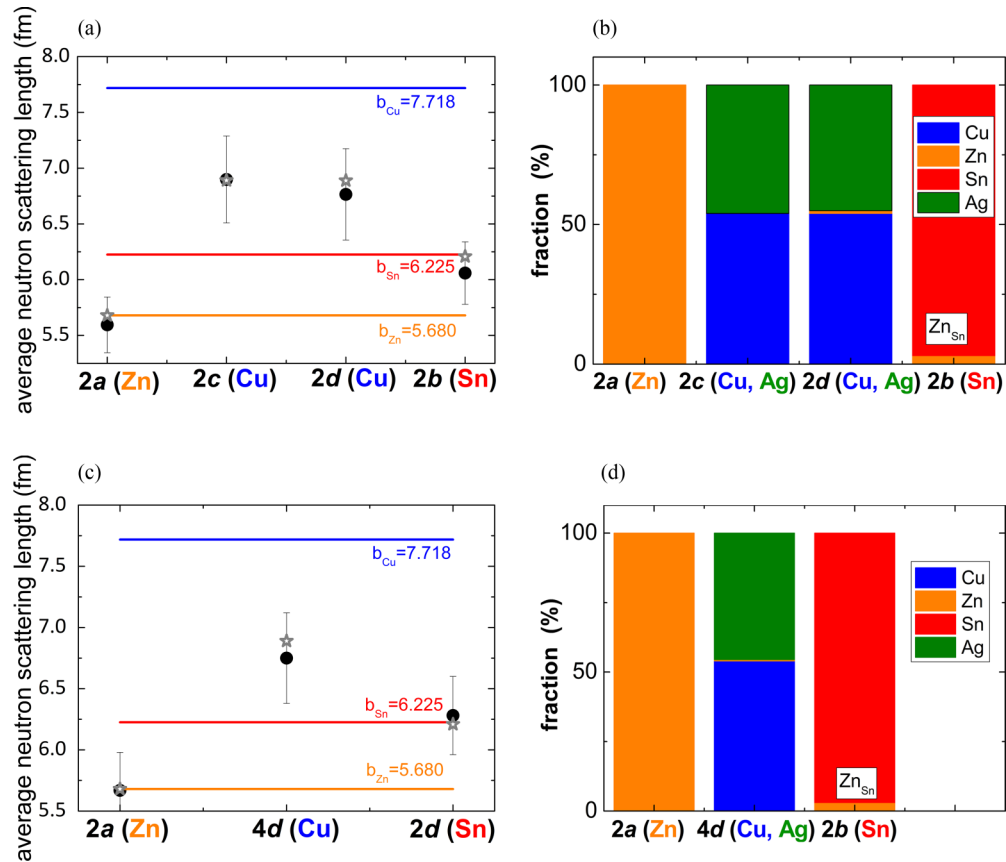


FIG. 3. (a) Average neutron-scattering length  $\bar{b}$  of the cation sites  $2a$ ,  $2c$ ,  $2d$ , and  $2b$ , assuming kesterite-type structure exemplarily shown for  $\text{Ag}_{0.91}\text{Cu}_{1.08}\text{Zn}_{1.03}\text{Sn}_{0.99}\text{Se}_4$  (full symbols: experimental values; stars: calculated values according to a cation distribution model); (b) resulting cation distribution in  $\text{Ag}_{0.91}\text{Cu}_{1.08}\text{Zn}_{1.03}\text{Sn}_{0.99}\text{Se}_4$  (Ag-46); (c) average neutron-scattering length  $\bar{b}$  of the cation sites  $2a$ ,  $4d$ , and  $2b$ , assuming stannite-type structure (full symbols: experimental values; stars: calculated values according to a cation distribution model); (d) resulting cation distribution in  $\text{Ag}_{0.91}\text{Cu}_{1.08}\text{Zn}_{1.03}\text{Sn}_{0.99}\text{Se}_4$  (Ag-46).

ison of the experimentally obtained values with the neutron-scattering lengths of copper, silver, zinc, and tin [Fig. 3(a)], it is already obvious that the average neutron-scattering length of the copper site  $2a$  is extremely decreased in comparison to the copper neutron-scattering length and is equal to the zinc neutron-scattering length which means that the  $2a$  position is completely occupied by  $\text{Zn}^{2+}$  [Fig. 3(b)]. The  $2c$  and  $2d$  positions where Cu/Zn disorder is usually present in compounds with the kesterite-type structure are occupied by  $\text{Ag}^+$  and  $\text{Cu}^+$  in proportions suggested by the chemical compositions [see Fig. 3(b)] instead. Only  $\text{Sn}^{4+}$  is located in the  $2b$  position as expected. All of the findings mentioned above are very strong indications of the stannite-type structure (space-group  $I\bar{4}2m$ ). An additional refinement of the powder pattern using the stannite-type structure with Zn on  $2a:(0,0,0)$ , Cu/Ag on  $4d:(0, \frac{1}{2}, \frac{1}{4})$ , Sn on  $2b:(\frac{1}{2}, \frac{1}{2}, 0)$ , and Se on  $8i:(x, x, z)$  Wyckoff positions as a starting model was performed. A lower value for both  $R_{\text{Bragg}}$  and  $\chi^2$  (e.g.,  $R_{\text{Bragg}} = 3.33$  instead of 4.14 and  $\chi^2 = 2.48$  instead of 2.69 in the case of Ag-46) was obtained. A slight presence of off-stoichiometry-type-related defects was detected as well. The resulting comparison of the experimentally obtained values with the neutron-scattering lengths of copper, silver, zinc, and tin [Fig. 3(c)] and cation distribution [Fig. 3(d)] are presented as well. The kesterite-type structure of AZTSe reported earlier was confirmed by

anomalous x-ray diffraction [29]. The paper concerning these results is in preparation and will be published separately [30].

The optoelectronic properties of the powders synthesized were measured by means of hyperspectral imaging, thus, allowing good statistics and providing representative data of the large volume of crystallite powder samples. From the diffuse reflectance data, the band gap of the  $(\text{Ag}_{1-x}\text{Cu}_x)_2\text{ZnSnSe}_4$  series has been calculated with Tauc plots using the Kubelka-Munk function [31] as shown in [Fig. 4(a)]. The band gap dependence on the composition is shown in Fig. 4(b). An

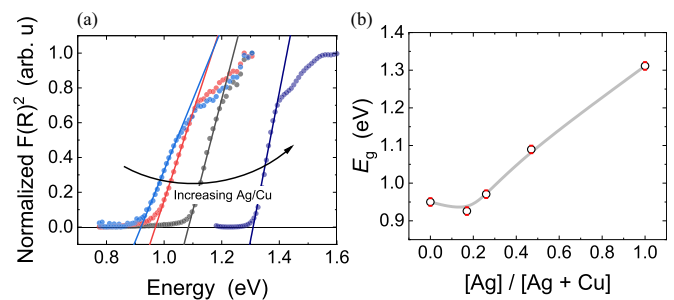


FIG. 4. (a) Tauc plots for the band-gap determination of the powders. (b) Band-gap values  $E_g$  as a function of the  $[\text{Ag}] / [\text{Ag} + \text{Cu}]$  ratio of the powders. The gray line is a guide for the eye.



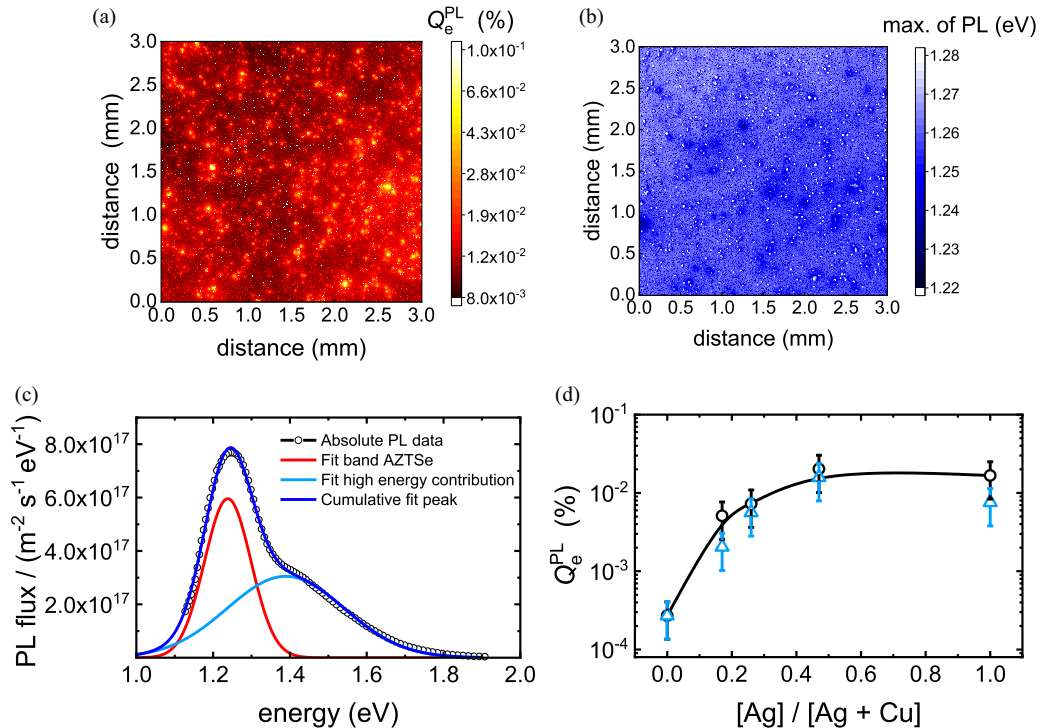


FIG. 5. (a) Map of the external PL quantum yield  $Q_e^{\text{PL}}$  and (b) of the energy of the center of the PL emission band of the  $\text{Ag}_2\text{ZnSnSe}_4$  powder. The pixel resolution in both maps is approximately  $10\ \mu\text{m}$  in diameter and an average grain area of about  $\sim 160\ \mu\text{m}^2$  is estimated from the BSE micrograph shown in Fig. 1(a) (see also the Supplemental Material [27]). A Gaussian fit was performed to construct the maps in every pixel and to extract  $Q_e^{\text{PL}}$  (from the area) and the PL maximum (from the center). For computational simplicity, the data with energies above 1.35 eV were masked to omit the contribution of the high-energy band and avoid multiple peak fits. (c) Absolute intensity PL spectrum of the  $\text{Ag}_2\text{ZnSnSe}_4$  powder. (d) External PL quantum yield  $Q_e^{\text{PL}}$  as a function of composition. The black symbols represent the upper limit for the values of  $Q_e^{\text{PL}}$  which have been calculated integrating the full PL spectrum (area of the cumulative fit in (c)). The blue symbols correspond to the lower bound estimated for  $Q_e^{\text{PL}}$  which has been calculated with the area of the Gaussian peak of the  $(\text{Ag}_{1-x}\text{Cu}_x)_2\text{ZnSnSe}_4$  band (red peaks in (c) and Fig. S3 of the Supplemental Material [27]). The black line is a guide for the eye.

initial decrease in the band gap energy is observed for the Ag-17 sample compared to CZTSe. Then, an increase in the  $E_g$  values with increasing the Ag/(Ag + Cu) ratio is found for  $x$  larger than  $\sim 0.2$ . The values are in agreement with the band gaps and bowing in the study reported by Gong *et al.* [15] showing that, for Ag contents above 50%, the optical band gap of the material approaches the optimal region for photovoltaic energy conversion.

To evaluate the potential of the synthesized compounds as absorbers for thin-film solar cells, absolute PL hyperspectral imaging has been performed on the  $(\text{Ag}_{1-x}\text{Cu}_x)_2\text{ZnSnSe}_4$  series. The advantage of imaging techniques for the optoelectronic characterization of the powders can be understood when looking at the maps shown in Figs. 5(a) and 5(b). The distribution of the external PL quantum yield ( $Q_e^{\text{PL}}$ ) measured over a  $3 \times 3\ \text{mm}^2$  of the  $\text{Ag}_2\text{ZnSnSe}_4$  powder can be seen in Fig. 5(a). The map shows local grain-to-grain variations in the  $Q_e^{\text{PL}}$  values. A statistical analysis based on a Gaussian distribution indicates a standard deviation of the  $Q_e^{\text{PL}}$  map around 30% (see the Supplemental Material [27]). As the luminescence yield depends on both minority carrier lifetime and charge carrier (doping) density, the local changes in  $Q_e^{\text{PL}}$  can arise from variations in either of these two quantities. Similarly, a map of the center of the emission band attributed to the

$\text{Ag}_2\text{ZnSnSe}_4$  phase is shown in Fig. 5(b). This map exhibits local differences in the energy of the PL maximum of up to 80 meV with an average value of 1.258 eV and a standard deviation of 11 meV (see histograms in the Supplemental Material [27]).

The average PL spectrum of the  $\text{Ag}_2\text{ZnSnSe}_4$  sample is presented in Fig. 5(c). The spectrum shows a PL band close to the band gap (1.31 eV determined by diffuse reflectance) accompanied by a higher-energy secondary peak. We attribute the dominant PL band of the ACZTSe samples to band-to-band (BB) or band-to-tail (BT) transition based on the comparison of the PL maximum and the band gap ( $E_g$ ) of the kesterites determined by diffuse reflectance (Table II). Based on this criterion, the PL emission of the lower Ag-containing samples is attributed to the BB transition [32]. The samples with higher Ag content exhibit a dominant PL band located 30–50 meV below the estimated band gap and it most likely originates from a BT type transition (see the Supplemental Material Fig. S3 [27]). The high-energy band observed in the spectrum of the AZTSe sample is likely to be secondary phases related, and it appears for all the Ag-containing powders studied (see the Supplemental Material [27]). This has been evaluated by synthesizing and measuring powders of  $\text{Ag}_8\text{SnSe}_6$  and ZnSe. We can discard that the

TABLE II. Summary of parameters obtained from the optoelectronic characterization performed in the powders. The  $Q_e^{\text{PL}}$  values shown in the table are the average of the upper and lower bounds shown in Fig. 5(d).

Ag/(Ag + Cu)	$Q_e^{\text{PL}}$ (%)	$E_g$ (eV)	Maximum of PL (eV)	$\Delta\mu_{SQ}$ (eV)	$\Delta\mu$ (eV)	$\Delta\mu/\Delta\mu_{SQ}$ (%)
1	$1.2 \times 10^{-2}$	1.31	1.25	1.05	0.82	78
0.46	$1.8 \times 10^{-2}$	1.08	1.05	0.84	0.61	73
0.26	$6.4 \times 10^{-3}$	0.96	0.95	0.73	0.48	66
0.17	$3.6 \times 10^{-3}$	0.92	0.92	0.69	0.42	61
0	$2.7 \times 10^{-4}$	0.94	0.94	0.79	0.38	53

high-energy contribution comes from the emission of the  $\text{Ag}_8\text{SnSe}_6$  which shows a photoluminescence emission peak centered at 0.83 eV (see the Supplemental Material [27]). On the other hand, the origin of the high-energy band could come from ZnSe in which we detect a PL signal centered at 1.27 eV from a transition possibly related to a defect level of this phase. It is important to highlight that the  $\text{Ag}_8\text{SnSe}_6$  and ZnSe phases which may segregate during the growth of the  $(\text{Ag}_{1-x}\text{Cu}_x)_2\text{ZnSnSe}_4$  powder are likely to lead to different defect properties compared to the reference powders and, therefore, contribute differently to the overall PL emission spectra. It is also worth commenting that the presence of  $\text{Ag}_8\text{SnSe}_6$  (found in all the Ag-containing samples of this paper) might be problematic in a solar cell due to its narrow band gap, particularly, if this phase is located close to the *pn* junction. However, this problem could potentially be overcome by a KCN chemical etching of the absorber layer [10].

The evolution of the external photoluminescence quantum efficiency  $Q_e^{\text{PL}}$  with the increasing Ag/(Ag + Cu) ratio is shown in Fig. 5(d) and indicates an increase by two orders of magnitude from  $\text{Cu}_2\text{ZnSnSe}_4$  to  $\text{Ag}_2\text{ZnSnSe}_4$ . As pointed out above, the photoluminescence yield (and, thus,  $Q_e^{\text{PL}}$ ) in low injection conditions depends on both the minority carrier lifetime and the doping density of the material. Therefore, the increase in the  $Q_e^{\text{PL}}$  observed for increasing silver content in the samples could, in principle, be due to an increase in the Shockley-Read-Hall (SRH) lifetime or to an increase in the intrinsic doping density. Although we were not able to measure the carrier density in these powder samples, we note that there have been several reports in the literature that clearly indicate a strong decrease in the intrinsic doping density with increasing silver content with up to four orders of magnitude lower values observed for  $\text{Ag}_2\text{ZnSnSe}_4$  than for  $\text{Cu}_2\text{ZnSnSe}_4$  [10]. This would indicate that the significant increase in  $Q_e^{\text{PL}}$  observed for the higher silver content is due to a strongly increased SRH lifetime caused by a reduction in nonradiative recombination via deep defects. Indeed, such increased lifetimes have been recently predicted for  $\text{Ag}_2\text{ZnSnSe}_4$  in a first-principles study of nonradiative recombination [33], which indicated that carrier capture and recombination induced by  $\text{Sn}_{\text{Zn}}$  antisite defects are significantly suppressed in this compound.

$Q_e^{\text{PL}}$  can be used to calculate the quasi-Fermi-level splitting and, thus, allows an estimation of maximum achievable  $V_{\text{OC}}$  in a solar cell following the approach from Ross [34]. The higher the  $Q_e^{\text{PL}}$ , the lower the  $V_{\text{OC}}$  deficit with respect to the ideal one at the Shockley-Queisser limit [34,35]. The

estimated values of  $\Delta\mu$  from  $Q_e^{\text{PL}}$  are shown in Table II along with the ideal  $\Delta\mu^{\text{SQ}}$  (Shockley-Queisser limit). The low Ag-containing samples (Ag-17 and Ag-26) show above 60% of the  $\Delta\mu^{\text{SQ}}$ , which is a  $\sim 10\%$  improvement with respect to the CZTSe powder. These values are comparable to the ones reported for the best kesterite solar cells [9,36,37]. Remarkably, the percentage of gain in maximum achievable  $V_{\text{OC}}$  with respect to the ideal  $V_{\text{OC}}$  increases by more than 20% for the mixed crystals with  $x = 0.46$  and  $x = 1$  compared to the  $\text{Cu}_2\text{ZnSnSe}_4$  end member. Such an increase in the measured quasi-Fermi-level splitting demonstrates that Ag incorporation in CZTSe can be a promising strategy to reduce the  $V_{\text{OC}}$  deficit of kesterite solar cells. A maximum achievable  $\Delta\mu$  of  $\sim 820$  meV is calculated for the pure Ag compound. This value of the quasi-Fermi-level splitting is more than 300 meV larger than the  $V_{\text{OC}}$  achieved in the best solar cell reported using  $\text{Ag}_2\text{ZnSnSe}_4$  as an absorber layer [38]. Since the quasi-Fermi-level splitting gives the achievable upper limit for the  $V_{\text{OC}}$ , additional losses must occur when functional layers and contacts are added in the devices as has been recently shown and discussed in detail for halide-perovskite solar cells [39,40]. One possible reason for the limited  $V_{\text{OC}}$  observed in silver-containing  $(\text{Ag}_{1-x}\text{Cu}_x)_2\text{ZnSnSe}_4$  solar cells is the fact that, in addition to low charge-carrier densities, a type conversion from *p*-type to *n*-type doping has been found for  $x < 0.1$ . Thus, conventional *pn*-junction device architectures commonly employed for chalcopyrite- or kesterite-type solar cells, which include a *n*-type window (zinc oxide or indium tin oxide) and a *n*-type buffer layer (CdS), are not expected to lead to good photoconversion properties. If *n*-type absorber layers are to be used, either a *np*-junction configuration with a *p*-type buffer/window layer or a *p-i-n*-type configuration with highly selective *n*- and *p*-type contact layers would have to be employed. At present, this poses a considerable challenge as there is a lack of suitable *p*-type conducting materials but indicates a promising direction for future research. The greatly improved radiative efficiencies in the  $(\text{Ag}_{1-x}\text{Cu}_x)_2\text{ZnSnSe}_4$  investigated in this paper indicate the possibility of increased photoconversion efficiencies in thin-film solar cells derived from kesterite/stannite-type materials than the current state of art.

#### IV. CONCLUSION

Detailed structural analysis of a  $(\text{Ag}_{1-x}\text{Cu}_x)_2\text{ZnSnSe}_4$  solid solution series was performed by means of neutron and x-ray diffraction. In contrast to previous assignments of the kesterite structure to  $\text{Ag}_2\text{ZnSnSe}_4$  and  $\text{Cu}_2\text{ZnSnSe}_4$ , we find

that mixed crystals with  $x = 0.17$  and  $0.46$  adopt the stannite-type structure, in this way, the possibility for Cu/Zn disorder formation is completely blocked.

The photoluminescence quantum yield  $Q_c^{PL}$  was found to increase with Ag content by up to two orders of magnitude compared to CZTSe. The high  $Q_c^{PL}$  measured in the AZTSe sample suggests that solar cells based on this compound with a  $V_{OC}$  larger than  $0.8$  V with a band gap of  $1.31$  eV could be, in principle, achieved.

## ACKNOWLEDGMENTS

The authors thank HZB for allocation of the neutron radiation beam time. The research leading to the presented results has been partially supported by the STARCELL Project as well as the INFINITE-CELL Project. These projects have received funding from the European Union's Horizon 2020 Research and Innovation Programme under the Marie Skłodowska-Curie Grant Agreements No. 720907 and No. 777968, respectively.

- 
- [1] S. K. Wallace, D. B. Mitzi, and A. Walsh, The steady rise of kesterite solar cells, *ACS Energy Lett.* **2**, 776 (2017).
- [2] S. Levchenko, J. Just, A. Redinger, G. Larramona, S. Bourdais, G. Dennler, A. Jacob, and T. Unold, Deep Defects in  $\text{Cu}_2\text{ZnSn}(\text{S}, \text{Se})_4$  Solar Cells with Varying Se Content, *Phys. Rev. Appl.* **5**, 024004 (2016).
- [3] *Identifying the Real Minority Carrier Lifetime in Nonideal Semiconductors: A Case Study of Kesterite Materials-Hages-2017, Advanced Energy Materials* (Wiley Online Library, Hoboken, NJ, 2017).
- [4] J. J. S. Scragg, J. K. Larsen, M. Kumar, C. Persson, J. Sendler, S. Siebentritt, and C. Platzer Björkman, Cu–Zn disorder and band Gap fluctuations in  $\text{Cu}_2\text{ZnSn}(\text{S}, \text{Se})_4$ : Theoretical and experimental investigations, *Phys. Status Solidi B* **253**, 247 (2016).
- [5] W.-C. Huang, S.-Y. Wei, C.-H. Cai, W.-H. Ho, and C.-H. Lai, The role of Ag in aqueous solution processed  $(\text{Ag}, \text{Cu})_2\text{ZnSn}(\text{S}, \text{Se})_4$  kesterite solar cells: antisite defect elimination and importance of Na passivation, *J. Mater. Chem. A* **6**, 15170 (2018).
- [6] S. G. Haass, C. Andres, R. Figi, C. Schreiner, M. Bürki, Y. E. Romanyuk, and A. N. Tiwari, Complex interplay between absorber composition and alkali doping in high efficiency kesterite solar cells, *Adv. Energy Mater.* **8**, 4 (2018).
- [7] C. J. Hages, N. J. Carter, and R. Agrawal, Generalized Quantum Efficiency Analysis for Non-Ideal Solar Cells: Case of  $\text{Cu}_2\text{ZnSnSe}_4$ , *J. Appl. Phys.* **119**, 14505 (2016).
- [8] H. Xin, S. M. Vorpahl, D. Collord, I. L. Braly, R. Uhl, B. W. Krueger, D. S. Ginger, and H. W. Hillhouse, Lithium-doping inverts the nanoscale electric field at the grain boundaries in  $\text{Cu}_2\text{ZnSn}(\text{S}, \text{Se})_4$  and increases photovoltaic efficiency, *Phys. Chem. Chem. Phys.* **17**, 23859 (2015).
- [9] A. D. Collord and H. W. Hillhouse, Germanium alloyed kesterite solar cells with low voltage deficits, *Chem. Mater.* **28**, 2067 (2016).
- [10] T. Gershon, Y. S. Lee, P. Antunez, R. Mankad, S. Singh, D. Bishop, O. Gunawan, M. Hopstaken, and R. Haight, Photovoltaic materials and devices based on the alloyed kesterite absorber  $(\text{Ag}_x\text{Cu}_{1-x})_2\text{ZnSnSe}_4$ , *Adv. Energy Mater.* **6**, 1 (2016).
- [11] M. Neuschitzer, J. Marquez, S. Giraldo, M. Dimitrievska, M. Placidi, V. I-R I. Forbes, A. Pérez-Rodríguez, and E. Saucedo,  $V_{OC}$  boosting and grain growth enhancing Ge-doping strategy for  $\text{Cu}_2\text{ZnSnSe}_4$  photovoltaic absorbers, *J. Phys. Chem. C* **120**, 9661 (2016).
- [12] C. J. Hages, M. J. Koeper, and R. Agrawal, Optoelectronic and material properties of nanocrystal-based cztsse absorbers with Ag-alloying, *Sol. Energy Mater. Sol. Cells* **145**, 342 (2016).
- [13] E. Chagarov, K. Sardashti, A. C. Kummel, Y. Seog Lee, R. Haight, and T. S. Gershon,  $\text{Ag}_2\text{ZnSn}(\text{S}, \text{Se})_4$ : A highly promising absorber for thin film photovoltaic cs, *J. Chem. Phys.* **144**, 104704 (2016).
- [14] S. Schorr, The crystal structure of kesterite type compounds: A neutron and X-ray diffraction study, *Sol. Energy Mater. Sol. Cells* **95**, 1482 (2011).
- [15] W. Gong, T. Tabata, K. Takei, M. Morihama, T. Maeda, and T. Wada, Crystallographic and optical properties of  $(\text{Cu}, \text{Ag})_2\text{ZnSnS}_4$  and  $(\text{Cu}, \text{Ag})_2\text{ZnSnSe}_4$  solid solutions, *Phys. Status Solidi C* **12**, 700 (2015).
- [16] L. E. Valle Rios, K. Neldner, G. Gurieva, and S. Schorr, Existence of off-stoichiometric single phase kesterite, *J. Alloys Compd.* **657**, 408 (2016).
- [17] G. Gurieva, L. E. Valle Rios, A. Franz, P. Whitfield, and S. Schorr, Intrinsic point defects in off-stoichiometric  $\text{Cu}_2\text{ZnSnSe}_4$ : A neutron diffraction study, *J. Appl. Phys.* **123**, 161519 (2018).
- [18] B. G. Mendis, K. P. McKenna, G. Gurieva, M. S. Rumsey, and S. Schorr, Crystal structure and anti-site boundary defect characterisation of  $\text{Cu}_2\text{ZnSnSe}_4$ , *J. Mater. Chem. A* **6**, 189, (2018).
- [19] G. Gurieva, D. M. Többens, M. Y. Valakh, and S. Schorr, Cu-Zn disorder in  $\text{Cu}_2\text{ZnGeSe}_4$ : a complementary neutron diffraction and Raman spectroscopy study, *J. Phys. Chem. Solids* **99**, 100 (2016).
- [20] P. Thompson, D. E. Cox, and J. B. Hastings, Rietveld refinement of Debye-Scherrer synchrotron X-ray data from  $\text{Al}_2\text{O}_3$ , *J. Appl. Crystallogr.* **20**, 79 (1987).
- [21] A. Franz and A. Hoser, Helmholtz-Zentrum Berlin für Materialien und Energie. E9: The Fine Resolution Powder Diffractometer (FIREPOD) at BER II, *J. Large-Scale Res. Facilities*, **3**, A103 (2017).
- [22] H. M. Rietveld, A profile refinement method for nuclear and magnetic structures, *J. Appl. Crystallogr.* **2**, 65 (1969).
- [23] J. Rodriguez-Carvajal, FULLPROFSUITE (2012).
- [24] P. Schöple, G. Gurieva, S. Giraldo, G. Martinez-Criado, C. Ronning, E. Saucedo, S. Schorr, and C. S. Schnorr, Discrepancy between integral and local composition in off-stoichiometric  $\text{Cu}_2\text{ZnSnSe}_4$  kesterites: A pitfall for classification, *Appl. Phys. Lett.* **110**, 043901 (2017).
- [25] R. Gunder, J. Márquez Prieto, G. Gurieva, T. Unold, and S. Schorr, Structural characterization of off-stoichiometric

- kesterite-type  $\text{Cu}_2\text{ZnGeSe}_4$  compound semiconductors: from cation distribution to intrinsic point defect density, *Cryst.Eng.Comm.* **20**, 1491 (2018).
- [26] V. F. Sears, Neutron scattering lengths and cross sections, *Neutron News* **3**, 26 (1992).
- [27] See Supplemental Material at <http://link.aps.org/supplemental/10.1103/PhysRevMaterials.4.054602> the Raman spectroscopy study, the detailed results on photoluminescence, and the details of the Rietveld refinement results, including Refs. [41–50].
- [28] S. Schorr, X-ray and neutron diffraction on materials for thin-film solar cells, in *Advanced Characterization Techniques for Thin Film Solar Cells*, edited by D. Abou-Ras, T. Kirchartz, and U. Rau, (Wiley-VCH Verlag GmbH, Weinheim, 2011), p. 347.
- [29] D. M. Többsens, R. Gunder, G. Gurieva, J. Marquardt, K. Neldner, L. E. Valle-Rios, S. Zander, and S. Schorr, Quantitative anomalous powder diffraction analysis of cation disorder in kesterite semiconductors, *Powder Diffr.* **31**, 168, (2016).
- [30] D. M. Többsens, G. Gurieva, and S. Schorr (unpublished).
- [31] P. Kubelka, New Contributions to the Optics of Intensely Light-Scattering Materials Part I, *J. Opt. Soc. Am.* **38**, 448 (1948).
- [32] M. V. Yakushev, J. Marquez-Prieto, I. Forbes, P. R. Edwards, V. D. Zhivulko, A. V. Mudryi, J. Krustok, and R. W. Martin, Radiative Recombination in  $\text{Cu}_2\text{ZnSnSe}_4$  Thin Films with Cu Deficiency and Zn Excess, *J. Phys. D: Appl. Phys.* **48**, 475109 (2015).
- [33] S. Kim, J. A. Márquez Prieto, T. Unold, and A. Walsh Upper limit to the photovoltaic efficiency of imperfect crystals from first principles, *Energy Environ. Sci.* **13**, 1481 (2020).
- [34] R. T. Ross, Some Thermodynamics of Photochemical Systems, *J. Chem. Phys.* **46**, 4590 (1967).
- [35] W. Shockley and H. J. Queisser, Detailed Balance Limit of Efficiency of P-N Junction Solar Cells, *J. Appl. Phys.* **32**, 510, (1961).
- [36] S. G. Haass, M. Diethelm, M. Werner, B. Bissig, Y. E. Romanyuk, and A. N. Tiwari, 11.2% efficient solution processed kesterite solar cell with a low voltage deficit, *Adv. Energy Mater.* **5**, 1500712 (2015).
- [37] J. Kim, H. Hiroi, T. K. Todorov, O. Gunawan, M. Kuwahara, T. Gokmen, D. Nair, M. Hopstaken, B. Shin, Y. S. Lee, W. Wang, H. Sugimoto, and D. B. Mitzi, High Efficiency  $\text{Cu}_2\text{ZnSn}(\text{S}, \text{Se})_4$  Solar Cells by Applying a Double  $\text{In}_2\text{S}_3/\text{CdS}$  Emitter, *Adv. Mater.* **26**, 7427 (2014).
- [38] T. Gershon, K. Sardashti, O. Gunawan, R. Mankad, S. Singh, Y. S. Lee, J. A. Ott, A. Kummel, and R. Haight, Photovoltaic device with over 5% efficiency based on an N-type  $\text{Ag}_2\text{ZnSnSe}_4$  Absorber, *Adv. Energy Mater.* **6**, 1601182 (2016).
- [39] M. Stolterfoht, C. M. Wolff, J. A. Márquez, S. Zhang, C. J. Hages, D. Rothhardt, S. Albrecht, P. L. Burn, P. Meredith, T. Unold, and D. Neher, Visualization and suppression of interfacial recombination for high-efficiency large-area pin perovskite solar cells, *Nat. Energy* **3**, 847 (2018).
- [40] M. Stolterfoht, P. Caprioglio, C. M. Wolff, J. A. Márquez Prieto, J. Nordmann, S. Zhang, D. Rothhardt, U. Hörmann, Y. Amir, A. Redinger, L. Kegelmann, F. Zu, S. Albrecht, N. Koch, T. Kirchartz, M. Saliba, T. Unold, and D. Neher, The impact of energy alignment and interfacial recombination on the open-circuit voltage of perovskite solar cells, *Energy Environ. Sci.* **12**, 2778 (2019).
- [41] M. Altosaar, J. Raudoja, K. Timmo, M. Danilson, M. Grossberg, J. Krustok, and E. Mellikov,  $\text{Cu}_2\text{Zn}_{1-x}\text{Cd}_x\text{Sn}(\text{Se}_{1-y}\text{S}_y)_4$  solid solutions as absorber materials for solar cells, *Phys. Status Solidi A* **205**, 167 (2008).
- [42] M. Guc, S. Levchenko, V. Izquierdo-Roca, X. Fontane, E. Arushanov, and A. Perez-Rodríguez, Polarized Raman scattering analysis of  $\text{Cu}_2\text{ZnSnSe}_4$  and  $\text{Cu}_2\text{ZnGeSe}_4$  single crystals, *J. Appl. Phys.* **114**, 193514 (2013).
- [43] N. B. Mortazavi Amiri and A. Postnikov, Electronic structure and lattice dynamics in kesterite-type  $\text{Cu}_2\text{ZnSnSe}_4$  from first-principles calculations, *Phys. Rev. B* **82**, 205204 (2010).
- [44] T. Gürel, C. Sevik, and T. Çağın, Characterization of vibrational and mechanical properties of quaternary compounds  $\text{Cu}_2\text{ZnSnS}_4$  and  $\text{Cu}_2\text{ZnSnSe}_4$  in kesterite and stannite structures, *Phys. Rev. B* **84**, 205201 (2011).
- [45] Y. Zhao, X. Han, B. Xu, W. Li, J. Li, J. Li, M. Wang, C. Dong, P. Ju, and J. Li, Enhancing open-circuit voltage of solution-processed  $\text{Cu}_2\text{ZnSn}(\text{S}, \text{Se})_4$  solar cells with Ag substitution, *IEEE J. Photovoltaics* **7**, 874 (2017).
- [46] G. Perna, M. Lastella, M. Ambrico, and V. Capozzi, Temperature dependence of the optical properties of ZnSe films deposited on quartz substrate, *Appl. Phys. A: Solids Surf.* **83**, 127 (2016).
- [47] Q. Chen, S. Bernardi, and Y. Zhang, Spatially resolved laser-induced modification Raman spectroscopy for probing the microscopic structural variations in the quaternary alloy  $\text{Cu}_2\text{ZnSnSe}_4$ , *Phys. Rev. Appl.* **8**, 034008 (2017).
- [48] V. G. Hadjiev, D. De, H. B. Peng, J. Manongdo, and A. M. Guloy, Phonon probe of local strains in  $\text{SnS}_x\text{Se}_{2-x}$  mixed crystals, *Phys. Rev. B* **87**, 104302 (2013).
- [49] W. Witte, R. Kniese, and M. Powalla, Raman investigations of  $\text{Cu}(\text{In}, \text{Ga})\text{Se}_2$  thin films with various copper contents, *Thin Solid Films* **517**, 867 (2008).
- [50] S. Rühle, Tabulated values of the Shockley–Queisser limit for single junction solar cells, *Sol. Energy* **130**, 139 (2016).